High Order Iterative Learning Control for Off-axis In-situ Rotation of Nanorobot inside SEM

Xiang Fu, Heng Zhang, Yuting Yang, Yang Wang*, and Song Liu*, *Member*, *IEEE*

***Abstract*—High-precision robotic rotational manipulation is crucial in fields such as nanomaterial defect detection, nanoscale 3-D observation, and nanomaterial twisting characterization. Conventional solutions predominantly depend on the alignment of the tracked object with the rotation axis, necessitating stringent robotic configuration and monopolizing multiple linear degrees of freedom (DOFs). Consequently, this significantly impedes the dexterity of nano-manipulation. In this study, we introduce an innovative nanorobotic manipulation system that incorporates a rotary nano-positioner affixed to the end joint. This configuration facilitates high-precision off-axis in-situ rotation, alleviating the constraints associated with conventional approaches. Additionally, we present methodologies for calibrating the rotation axis and quantifying misalignment between the target point and the rotation axis, pivotal for establishing an accurate kinematic model. Subsequently, we propose a novel Kalman filter-based iterative learning control method that capitalizes on information derived from previous operational trials to enhance response in subsequent iterations, thereby achieving high-precision in-situ rotation. Experimental validation, including comparisons with PID control and model predictive control, demonstrates the strategy's stability, reliability, and superiority. Our contribution lies in three aspects: Firstly, the proposed method mitigates the need for stringent robotic configuration on the rotation axis and avoids monopolization of linear DOFs. Secondly, the innovative application of the image Jacobian matrix technique in the calibration of kinematic model parameters is demonstrated. Thirdly, the effective utilization of repetitiveness in rotation manipulation represents a novel aspect in the control of nanorobots.**

***Index Terms*—Off-axis rotation, In-situ nanomanipulation, Nanorobotics, SEM, Iterative learning control**

I. INTRODUCTION

ROBOTIC nanomanipulation technique inside scanning electron microscope (SEM) holds immense promise in field of material science[1-6], cell biology [8-10], and semiconductor[11], as it is capable of providing precise spatial displacement via linear translation and facilitating accurate adjustment in object posture and multidirectional observation via rotary manipulation. These capabilities have proven highly beneficial for various studies, including, nanoscale device fabrication [7], cell manipulation [8-10] and nanoelectromechanical systems (NEMS) manufacturing [11], nanomaterial defect detection [12], 3-D nanoscale observation [13-14] and nanomaterial twisting characterization [15-16].

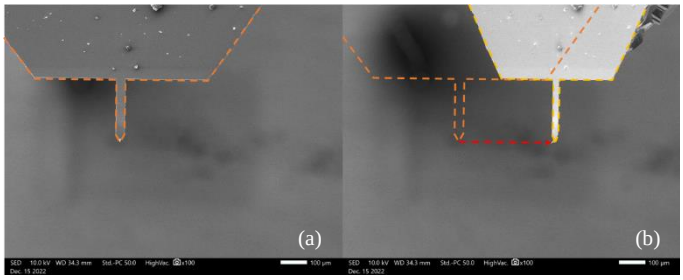

Fig. 1. Position shift after rotation of 50° caused by misalignment, where the magnification is 100, and the scale bar is 100 μm. (a) SEM image of cantilever before rotation; (b) SEM image of cantilever after rotation of 50°.

Compared with linear motion, rotary motion presents a multitude of challenges due to the inherent characteristic wherein the end-effector consistently maintains a spatial distance from the rotation axis. This spatial relationship results in significant mechanical misalignment at the microscale, even when the rotation angle is small. Such misalignment becomes problematic when conducting sustained rotational manipulation, as it will cause the end effector to move out of the field of view (FoV) or depth of focus. As depicted in Fig. 1, a substantial position shift on the order of hundreds micron arises during rotation. This displacement necessitates compensation. Such compensation is nontrivial while SEM provides merely 2D images and thereby lacks of depth information which is crucial for compensation in rotary manipulation to maintain within DoF. The depth information on optical axis can be estimated via depth from focus [17-18]. However, in fast scanning mode, SEM images manifest substantial noise, potentially exerting adverse effects on estimations. Furthermore, the persistent variations in the posture of the end effector during rotation, particularly at commonly employed nanomanipulation magnifications (e.g., 1000x), result in the mismatch of the edge information depicted in the mapped image. This renders conventional sharpness evaluation metrics unreliable, given the dynamic

This work was supported in part by the National Natural Science Foundation of China under grant 623043321. (Xiang Fu and Heng Zhang contribute equally to this work.) (Corresponding author: *Yang Wang* and *Song Liu*)

X. Fu, H. Zhang, Y. Yang, Y. Wang, and S. Liu are with the School of Information Science and Technology, ShanghaiTech University, shanghai, China (e-mail: fuxiang2022, zhangheng1, yangyt1, wangyang4, liusong@shanghaitech.edu.cn).

nature of edge features. Consequently, these variations pose challenges to the accuracy of depth estimation. Hence, relying on focal depth for estimating positions along the optical axis is not feasible due to its inherent coarseness and lack of practicality.

Significant efforts have been devoted to addressing this depth estimation challenge. One intuitive solution involves the assembly of multiple lenses in a microscope with subsequent center alignment. For instance, mounting optical microscope (OM) on the side of SEM chamber can offer an additional side view, facilitating the depth estimation of end-effector inside SEM, and thereby enabling nanomanipulation [19]. However, the installation of an OM significantly limits the chamber space, and potentially impact the quality of SEM imaging. Alternatively, centering end-effector has emerged as a recent technique to align samples with the rotation axis, thereby minimizing significant displacements and circumvent the necessity of the depth estimation. For instance, the static triple-image alignment (TIA) methods developed by Haojian et al [20-21] and their extended dynamic version [22], in which two linear nano-positioners are orthogonally mounted on the rotary nano-positioner. By assuming that the rotation axis is orthogonal to the two linear axes, these alignment methods simplify the modeling process but concurrently introduce inherent model errors. Moreover, the alignment method requires the utilization of two linear nano-positioners exclusively designed for centering, thereby impeding the execution of intricate rotary manipulations, such as the tension test of micro-materials. In summary, neither incorporating supplementary vision hardware within the chamber nor affixing extra linear nano-positioners onto a rotary nano-positioner proves to be a viable solution for addressing the challenges of in-situ nanomanipulation. This underscores the need for online compensation strategies to address off-axis rotational manipulation under SEM.

To address this objective, we reframe the issue from a control standpoint [23], specifically modeling online compensation strategies for off-axis rotational manipulation as a trajectory tracking control problem. In order to achieve high-precision trajectory tracking, the control strategy must effectively handle model uncertainties and external disturbances [24]. Consequently, conventional solutions prevalent in the field of nanoscale positioning control, such as sliding mode control [25, 28], neural networks [26], and various robust adaptive control methods [27, 30], cannot be directly applied to the off-axis rotation problem due to their restrictive assumptions and suboptimal performance. For example, the precision of model information required in [28] and the technique developed in [30] are inadequate for addressing substantial external disturbances. Conversely, we observe that numerous nanoscale positioning applications, including the in-situ manipulation under consideration, entail repetitive desired tracking trajectories [23, 29]. In such scenarios, Iterative Learning Control (ILC) emerges as a promising solution [31].

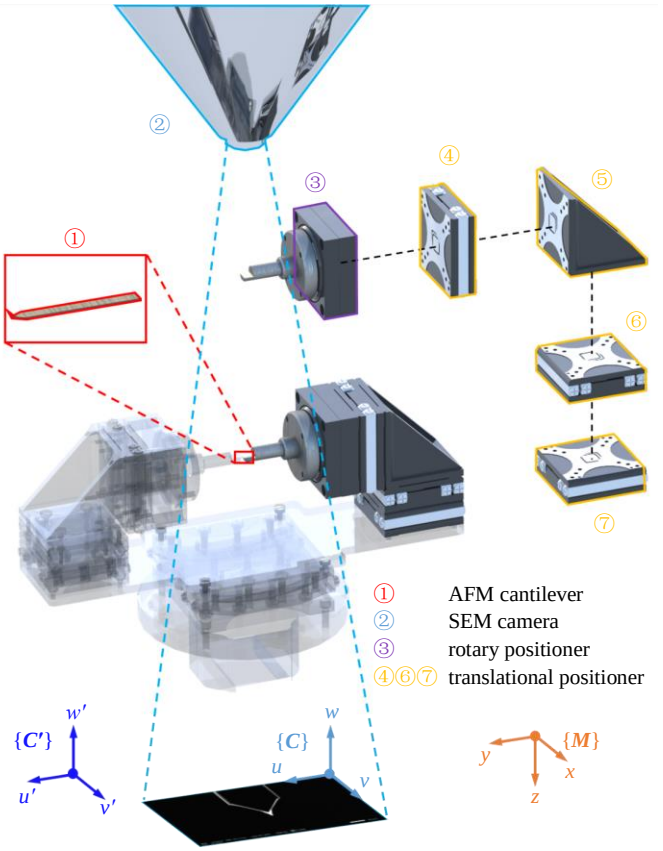

Fig. 2. Basic configuration of the nanorobotic manipulation system. A rotational nanorobotic system unit contains three translational DOFs and one rotary DOF.

In this paper, we present a nanomanipulation system featuring a rotary nano-positioner mounted at the end joint, as illustrated in Fig. 2. Importantly, our approach doesn't monopolize the linear DoFs, thereby reducing configuration cost, and it does not demand a strict adherence to a specific system configuration for the rotation axis. We also provide methods for calibrating the rotation axis and measuring misalignment between the target point and the rotation axis, which are essential for establishing appropriate state space model. Based on the identified model, we propose a Kalman-filter-based iterative learning control method to desired trajectory tracking, i.e. in-situ rotation. By exploiting the repeatability of the off-axis in-situ rotation, ILC leverages information from previous operational trials to enhance the response in the next iteration. Consequently, system performance can be improved through iterations [32]. To enable the system to track the desired trajectory faster and more accurately, this paper proposes a high-order iterative learning control approach [33] which is the first time utilized in nanorobots control. In the in-situ rotating experiment, the results demonstrate a significant reduction in the average position shift of the target object, decreasing from 417.058 μm to 1.374 μm, reflecting a remarkable improvement of 99.671% under the proposed control method.

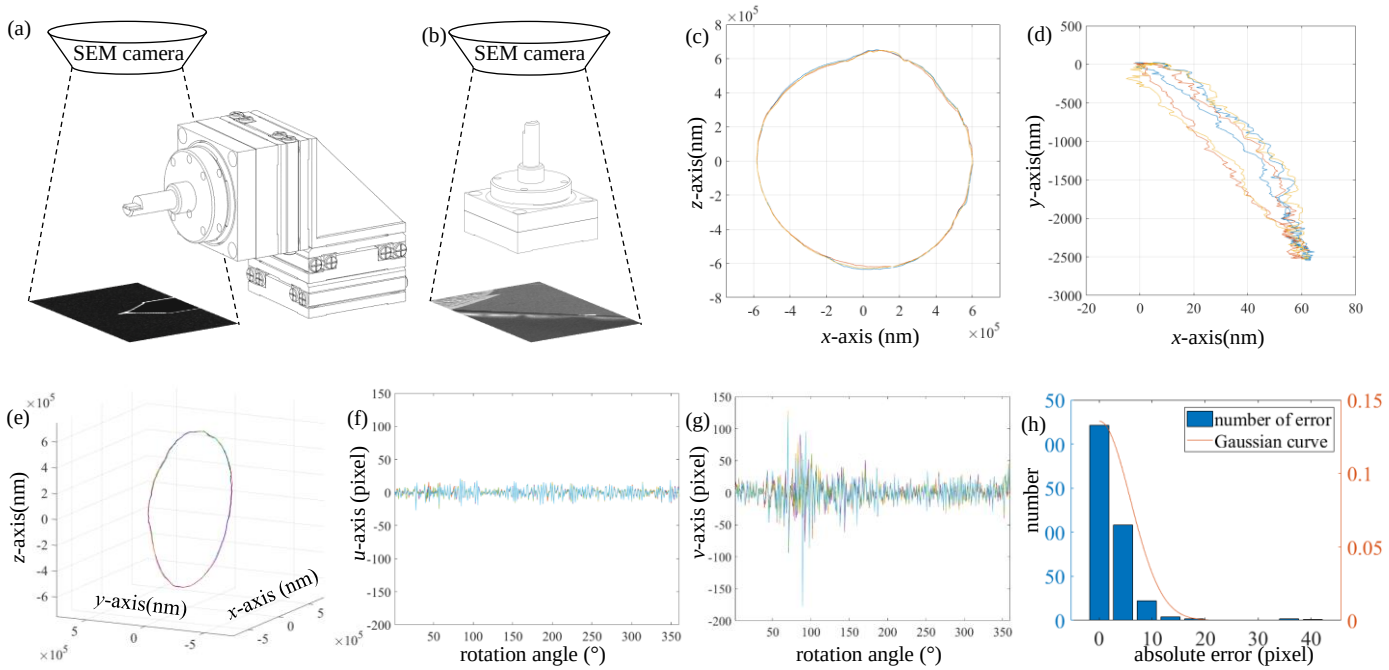

Fig. 3. (a) Observation of cantilever in side view. (b) Observation of cantilever in front view. (c) Displacement on *x*- and *z*-axis. (d) Displacement on *x*- and *y*-axis. (e) Displacement in 3D motion space {$\boldsymbol{M}$}. (f) Displacement on *u*-axis for each step in different revolutions. (g) Displacement on *v*-axis for each step in different revolutions. (h) Histogram for the absolute error on displacement in each step and a fitted gaussian curve. In each figure, lines in different colors represent different rotations.

The rest of this paper is organized as follows. The nanorobotic manipulation system configuration and displacement investigation is first discussed in Section II. Afterward, in Section III, the kinematics of the nanorobotic system and the calibration method for misalignment and rotation axis is clarified. Then, in Section IV, the designed controller based on iterative learning framework is proposed, including Kalman filtering-based observer and stability analysis. The reliability and availability of the proposed approach is validated by well-designed experiments and is compared with the state-of-the-art methods. Finally, this article makes the conclusion in Section VI.

II. Rotational Nanorobotic Manipulation System Configuration

A. Rotational Nanorobotic Manipulation System

Configuration of the proposed nanorobotic manipulation system is illustrated in Fig. 2, which consists of an SEM camera and four nanopositioners that provide three translational DoFs and one rotary DoF. Within the vacuum chamber of SEM, the three linear nanopositioners are orthogonally mounted, and one rotary nanopositioner is utilized at the end of the nanorobotic manipulation arm. The translational nano-positioner provides a precision of 1 nm, while the rotary nano-positioner achieves a high angle precision of up to 1°, offering highly reliable feedback for control movements. A top-view camera is employed to capture 2D images of the workspace.

Fig. 2 also portrays the establishment of three coordinate systems for the nanorobotic manipulation system. The 3D motion space {$\boldsymbol{M}$} is defined on the base of robotics system, with *x*-, *y*-, *z*-axes aligned with the orientations of three translational nanopositioners. The image space {$\boldsymbol{C}$} is established on the imaging plane of SEM camera, where *u*- and *v*-axes represent two axes of SEM image and *w*-axis represents the optical axis, which is orthogonal to *u*-, *v*-axes. The last coordinate system {$\boldsymbol{C'}$}, serves as an auxiliary uniform coordinate system introduced for the convenience of the rotational axis calibration. The orientation of the axes of {$\boldsymbol{C'}$} is chosen to be same as that of {$\boldsymbol{C}$} while the scale in {$\boldsymbol{C'}$} is set to be the same as in {$\boldsymbol{M}$}. In addition to the coordinate systems in Fig. 2, the coordinate system {$\boldsymbol{E}$} is designed for modeling simplification and will be introduced in the Section III. *A*.

The manipulation system incorporates one camera, that transforms the incremental translational motion of target object from the 3D Cartesian space {$\boldsymbol{M}$} into its representation in the image space {$\boldsymbol{C}$}. To obtain an accurate motion model of the observed object, pre-calibration of the parameters of the vision system, specifically the image Jacobian matrix $\boldsymbol{J_C}$, is necessary. For magnifications exceeding 500, the image projection exhibits affine transformation characteristics due to the limited depth of focus. Consequently, at a certain magnification, the image Jacobian matrix remains constant in SEM images, allowing for pre-calibration.

It is worth noting that the rotation axis is not considered as the *y*-axis in {$\boldsymbol{M}$}, despite its close proximity. To facilitate the calibration of the rotational axis, a normalized transformation matrix $\boldsymbol{J_{C'}^*}$ is employed to convert the motion space {$\boldsymbol{M}$} into the system {$\boldsymbol{C'}$}. The specific orientation vectors are calibrated in section III. *C* to ensure the accuracy of the system model.

B. Displacement During Robot Rotation

A comprehensive understanding of the displacement of the observed object during robot rotation is essential to enhance effective compensation for in-situ nanomanipulation under SEM. First, under SEM, we obtain the trajectories of cantilever mounted on the rotary nano-positioner from two different angles of view, as depicted by Fig. 3 (a)–(d). Then, the complete 3D trajectory of cantilever in {$\boldsymbol{M}$} coordinates, illustrated in Fig. 3 (e), can be calculated as follows:

$$\boldsymbol{x}_T(t) = \boldsymbol{x}_T(t-1) + (\boldsymbol{J}_{SF}{}^T \boldsymbol{J}_{SF})^{-1} \boldsymbol{J}_{SF}{}^T (\boldsymbol{y}_T(t) - \boldsymbol{y}_T(t-1)) \quad (1)$$

where $\boldsymbol{x}_T$ represents the three-dimensional spatial position in {$\boldsymbol{M}$} coordinates, $\boldsymbol{J}_{SF}$ is the Jacobian matrix that maps from the image systems in the side view and front view to the spatial motion space, and $\boldsymbol{y}_T$ is a 4 × 1 column vector formed by the position on two image planes.

As illustrated in Fig. 3 (c)-(d), the displacement of cantilever during rotation can be simplified as an orbit around a rotation axis, although the orbit was not perfect circle and polluted by subtle yet nanoscale biased noise. The noise primarily originates from the previously mentioned mechanical misalignment, and its impact is nonnegligible when precise off-axis in-situ rotation is required. For modelling simplicity, the trajectory is treated as combination of a circle and a perturbation noise.

To achieve a more precise calibration of the cantilever's trajectory, it is imperative to employ high magnification to minimize measurement noise. However, the presence of mechanical misalignment poses a challenge, as rotation manipulation under high magnification may lead to the cantilever exceeding the limited field of view. Consequently, a delicate balance between the field of view and magnification is crucial, and pre-synthesis compensation will aid in keeping the cantilever within the field of view. The calibrated 3D trajectory in {$\boldsymbol{M}$} serves as a valuable reference for implementing such compensation. Nevertheless, achieving high-precision in-situ rotation through compensation is limited, as the nanometer-scale displacement of the cantilever varies slightly in different rounds of rotation. The inconsistency in the observed trajectories arises from the presence of additional biased random noise in each rotation control step, caused by mechanical and measurement inaccuracy. The comparison results of multiple rotations are depicted in Fig. 3 (f)–(g), where differently colored curves represent displacement along the *u* and *v*-axes in different rounds of rotation. The distribution of the random noise, illustrated in Fig. 3 (h), exhibits characteristics of a Gaussian distribution with a mean absolute error approximately equal to 4.5070 pixels, equivalent to about 900 nm on average, and a standard deviation of 3.7930 pixels. The additional random noise in each step is modeled as Gaussian noise, and thus, the Kalman filter is implemented as the observer of the 3D trajectory of the cantilever. Further details will be provided in Section IV. *B*.

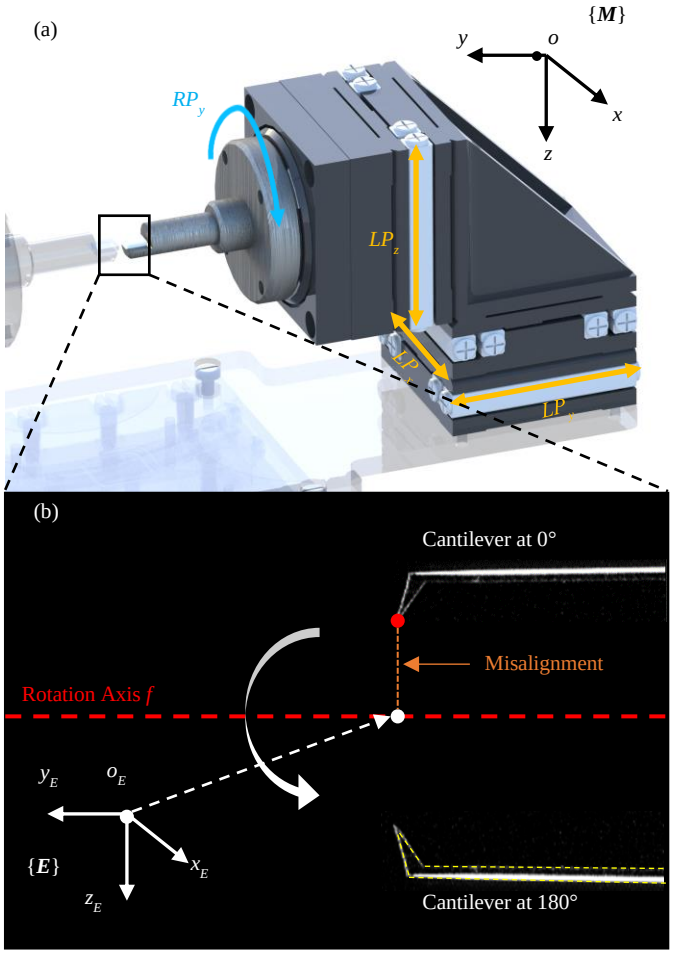

Fig. 4. (a) Diagram of specific nanorobotic configuration. (b) Manifested illustration of the setting near cantilever.

III. Modeling and Calibration

We begin by the kinematics of the nanorobotic manipulation system, followed by the calibration of misalignment and rotation axis.

A. Kinematics of the Nanorobotic Manipulation System

As shown in Fig. 4, a specific nanorobotic configuration is established, and the coordinate system {$\boldsymbol{E}$} is situated on the initial rotation axis. This implies that as the linear nanorobot moves, the origin of {$\boldsymbol{E}$} remains fixed in {$\boldsymbol{M}$}. The orientation vectors in {$\boldsymbol{E}$} are aligned with those in {$\boldsymbol{M}$}. The introduction of coordinate system {$\boldsymbol{E}$} eliminates the potential spatial offsets, which is a vector pointing from the origin of {$\boldsymbol{E}$} to the tracked feature point, such as the cantilever tip, indicated by the red dot in the Fig. 4 (b).

In the coordinate {$\boldsymbol{E}$}, disregarding the additional random noise discussed in Section II. *B*, the position of the tracked feature point, manipulated by nanopositioners, can be formulated as:

$$\boldsymbol{X} = \begin{bmatrix} P_x \\ P_y \\ P_z \end{bmatrix} = \boldsymbol{R}(f,\theta) \begin{bmatrix} \Delta x_f \\ \Delta y_f \\ \Delta z_f \end{bmatrix} + \begin{bmatrix} u_x \\ u_y \\ u_z \end{bmatrix} \quad (2)$$

where $\boldsymbol{X} = [P_x, P_y, P_z]^T$ is the position of feature point on the end-effector, $[\Delta x_f, \Delta y_f, \Delta z_f]^T$ denotes the primary mechanical misalignment which is identical for each revolution, $[u_x, u_y, u_z]^T$ is the linear motion of three translational nanopositioners, and $\boldsymbol{R}(f, \theta)$ is the standard rotation matrix around the rotation axis f about rotation angle θ, which can be expressed as:

$$\boldsymbol{R}(f,\theta) = \begin{bmatrix} f_x f_x v\theta + c\theta & f_y f_x v\theta - f_z s\theta & f_z f_x v\theta + f_y s\theta \\ f_x f_y v\theta + f_z s\theta & f_y f_y v\theta + s\theta & f_z f_y v\theta - f_x s\theta \\ f_x f_z v\theta - f_y s\theta & f_y f_z v\theta + f_x s\theta & f_z f_z v\theta + s\theta \end{bmatrix} \quad (3)$$

where $c\theta$ and $s\theta$ are the cosine and sine of the rotation angle θ, respectively; $v\theta$ denotes $vers\theta$, defined as $(1 - \cos\theta)$; the vector $[f_x, f_y, f_z]^T$ corresponds to the normalized orientation vector of the rotation axis f in the motion space $\{\boldsymbol{M}\}$, which will be measured in section III. *C*.

Next, take the control steps and the additional random noise into account, the kinematic model of the nanorobotic manipulation system (i.e. the transformation governing equation of the position of feature point form the instant t - 1th step to t^{th} step) is expressed as follows:

$$\begin{cases} \boldsymbol{X}_t = \boldsymbol{R}(f,\Delta\theta)\boldsymbol{X}_{t-1} + \boldsymbol{u}_t + (\boldsymbol{I} - \boldsymbol{R}(f,\Delta\theta))\sum_{n=0}^{t-1}\boldsymbol{u}_n + \boldsymbol{\delta}_t \\ \boldsymbol{X}_t = \begin{bmatrix} P_x^t & P_y^t & P_z^t \end{bmatrix}^T, \boldsymbol{u}_t = \begin{bmatrix} u_x^t & u_y^t & u_z^t \end{bmatrix} \end{cases} \quad (4)$$

where, at t^{th} time step, the state $\boldsymbol{X}_t$, control input $\boldsymbol{u}_t$ and disturbance input $\boldsymbol{\delta}_t$ separately represent the spatial position of the observed object (cantilever), the translation motion of the nano-positioners, and the influence brought by the additional random noise. $\Delta\theta$ is the rotation angle for each step which is constant during in-situ rotating control. Note that $\boldsymbol{R}(f, \Delta\theta)$ is denoted as $\boldsymbol{R}$ in the following expressions for simplicity.

This kinematic model of the nanomanipulation system illustrates the mathematical basis for compensating the displacement of the feature point by the nanorobot during the rotation process. With reference to Figure 3, it is evident that the constant vector $[\Delta x_f, \Delta y_f, \Delta z_f]^T$ representing the misalignment between the target point and the rotation axis as well as the vector $[f_x, f_y, f_z]^T$ obtained by the calibration of the rotation axis are crucial for the correctness of the kinematic model. In this context, this misalignment corresponds to the position of the feature point in $\{\boldsymbol{E}\}$, since $\{\boldsymbol{E}\}$ is the coordinate system established on the rotation axis, and its directional vectors align with those in $\{\boldsymbol{M}\}$. Subsequently, we will pre-calibrate the misalignment and rotation axis using the methods described in Sections III. *B* and III. *C*.

B. Alignment Error Estimation

In contrast to scenarios involving macroscale manipulation, the determination of absolute position becomes elusive in the microscale. In nanorobotic manipulation within SEM, only 2D SEM images are available, lacking depth information along the optic axis. Consequently, the measurement of misalignment poses a significant challenge. To address this issue, a systematic procedure for estimating misalignment has been developed as follows.

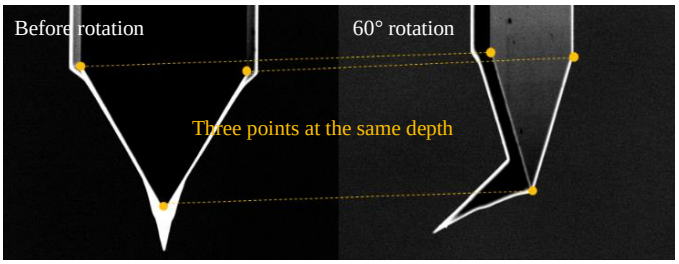

Fig. 5. An example of finding three points at the same depth, and the rotation axis is estimated with point feature matching between before and after certain rotation.

First, multiple rotation trials are conducted to generate SEM images with varying rotary increments. The image Jacobian matrix $\boldsymbol{J}_C$, as defined in [34], is introduced here for projecting from 3D motion space to the u-v image plane in $\{\boldsymbol{C}\}$. The image Jacobian matrix can be pre-calibrated to establish a correspondence between three motion axes and two image plane axes. At high magnification, the pre-calibrated $\boldsymbol{J}_C$ can be considered accurate and time-invariant. The feature increment is then calibrated for each rotation operation through:

$$\boldsymbol{J}_C(\boldsymbol{R} - \boldsymbol{I})\begin{bmatrix} \Delta x_f \\ \Delta y_f \\ \Delta z_f \end{bmatrix} = \begin{bmatrix} \Delta u \\ \Delta v \end{bmatrix} \quad (5)$$

where $[\Delta x_f, \Delta y_f, \Delta z_f]^T$ is the to-be-calculated misalignment about the rotation axis f, $\boldsymbol{I}$ is an identity matrix, and $[\Delta u, \Delta v]^T$ is the feature incremental motion in image space. $\boldsymbol{R}$ is the rotation matrix about $\Delta\theta$ over the rotation axis f.

With several rotation trials of the same angle, the expressions can be combined by:

$$\begin{bmatrix} \boldsymbol{J}_C \\ \boldsymbol{J}_C\boldsymbol{R} \\ \cdots \\ \boldsymbol{J}_C\boldsymbol{R}^{N-1} \end{bmatrix}(\boldsymbol{R} - \boldsymbol{I})\begin{bmatrix} \Delta x_f \\ \Delta y_f \\ \Delta z_f \end{bmatrix} = \begin{bmatrix} \Delta uv_1 \\ \Delta uv_2 \\ \cdots \\ \Delta uv_N \end{bmatrix} \quad (6)$$

where N is the number of rotary motion trials.

Secondly, given that $\boldsymbol{R}$, a rotation matrix about rotary angle $\Delta\theta$ around rotation axis f, is an orthogonal matrix processing an eigenvalue of 1, $(\boldsymbol{R} - \boldsymbol{I})$ features an eigenvalue of zero, indicating its singular nature. Therefore, the misalignment vector $[\Delta x_f, \Delta y_f, \Delta z_f]^T$ cannot be calculated directly using the matrix inverse. But the matrix preceding $(\boldsymbol{R} - \boldsymbol{I})$ is of full rank, then rotational motion of the feature point in motion space $\{\boldsymbol{M}\}$ can be estimated via:

$$(\boldsymbol{R} - \boldsymbol{I})\begin{bmatrix} \Delta x_f \\ \Delta y_f \\ \Delta z_f \end{bmatrix} = \begin{bmatrix} \boldsymbol{J}_C \\ \boldsymbol{J}_C\boldsymbol{R} \\ \cdots \\ \boldsymbol{J}_C\boldsymbol{R}^{N-1} \end{bmatrix}^{-1}\begin{bmatrix} \Delta uv_1 \\ \Delta uv_2 \\ \cdots \\ \Delta uv_N \end{bmatrix} \quad (7)$$

The general solution of the misalignment is shown by:

$$\begin{cases} \begin{bmatrix} \Delta x_f \\ \Delta y_f \\ \Delta z_f \end{bmatrix} = \begin{bmatrix} \Delta x_0 \\ 0 \\ \Delta z_0 \end{bmatrix} + m \begin{bmatrix} f_x \\ f_y \\ f_z \end{bmatrix} \\ \begin{bmatrix} \Delta x_0 \\ \Delta z_0 \end{bmatrix} = \left(\boldsymbol{R}-\boldsymbol{I}\right)_{2\times 2}^{-1} \left(\begin{bmatrix} \boldsymbol{J_C} \\ \boldsymbol{J_C R} \\ \cdots \\ \boldsymbol{J_C R}^{N-1} \end{bmatrix}^{-1} \begin{bmatrix} \Delta u v_1 \\ \Delta u v_2 \\ \cdots \\ \Delta u v_N \end{bmatrix} \right)_{2\times 2} \end{cases} \tag{8}$$

where the operation denoted by $[\text{-}]_{2\times2}$ involves removing both the middle column and the middle row from the original 3×3 matrix, resulting in the formation of a new 2×2 matrix. m represents an arbitrary constant, signifying that the general solution lies along a line parallel to the rotation axis.

Finally, during rotation, the movement of the feature point in 3D motion space can be calculated as:

$$\begin{aligned} \begin{bmatrix} \Delta x \\ \Delta y \\ \Delta z \end{bmatrix} &= (\boldsymbol{R}-\boldsymbol{I}) \begin{bmatrix} \Delta x_f \\ \Delta y_f \\ \Delta z_f \end{bmatrix} = (\boldsymbol{R}-\boldsymbol{I}) \begin{bmatrix} \Delta x_0 \\ 0 \\ \Delta z_0 \end{bmatrix} + m(\boldsymbol{R}-\boldsymbol{I}) \begin{bmatrix} f_x \\ f_y \\ f_z \end{bmatrix} \\ &= (\boldsymbol{R}-\boldsymbol{I}) \begin{bmatrix} \Delta x_0 \\ 0 \\ \Delta z_0 \end{bmatrix} \end{aligned} \tag{9}$$

The motion of the feature point is calculated with the misalignment $[\Delta x_f, \Delta y_f, \Delta z_f]^{\mathrm{T}}$, which is equal to the motion estimation with $[\Delta x_0, 0, \Delta z_0]^{\mathrm{T}}$. Therefore, $[\Delta x_f, \Delta y_f, \Delta z_f]^{\mathrm{T}}$ can be estimated with $[\Delta x_0, 0, \Delta z_0]^{\mathrm{T}}$.

C. Rotation Axis Estimation

When our nanorobotic manipulation system rotates the end effector, noticeable displacements along the u-axis in SEM images within the image space $\{\boldsymbol{C}\}$ occur. These displacements result from aforementioned mechanical misalignment, leading to inaccuracies in our kinematic model and consequently introducing trajectory errors in the in-situ rotational motion. Therefore, to achieve high-precision off-axis rotational motion, we cannot crudely assume that the direction of the rotation axis coincides with the y-axis of the motion space $\{\boldsymbol{M}\}$. A precise pre-calibration of the rotation axis is required. In this paper, the rotation axis f is characterized by its normalized orientation vector $\boldsymbol{f}$ in a specific coordinate system, for instance, $\boldsymbol{f_M}$ is a normalized orientation vector of the rotation axis f in $\{\boldsymbol{M}\}$.

First, we recall the auxiliary coordinates $\{\boldsymbol{C'}\}$ introduced in Section II. *A*. It serves as an intermediary coordinate system between the motion space $\{\boldsymbol{M}\}$ and the image space $\{\boldsymbol{C}\}$, maintaining orthogonally to meet the assumption in (3) while containing orientation information from $\{\boldsymbol{C}\}$ for scaling. To transfer the motion in space $\{\boldsymbol{M}\}$ to the coordinate system $\{\boldsymbol{C'}\}$ and extending the optical axis into the image space, we introduce the transformation matrix $\boldsymbol{J_{C'}}^*$ and the transformation matrix $\boldsymbol{J_C}^*$ which is extended from the image Jacobian matrix $\boldsymbol{Jc}$. The matrix $\boldsymbol{J_{C'}}^*$ is an orthogonal transformation matrix with the first row vector and the third row vector orientations similar to the image Jacobian matrix $\boldsymbol{J_C}$ and the second row vector as the cross product of the first and third row vectors. The matrix $\boldsymbol{J_C}^*$ is an orthogonal transformation matrix with the first row vector and the second row vector same as the image Jacobian matrix $\boldsymbol{J_C}$ and the third row vector as the cross product of the first and second row vectors. The matrix $\boldsymbol{J_{C'}}^*$ and the matrix $\boldsymbol{J_C}^*$ can be expressed as follows

$$\boldsymbol{J_{C'}}^* = \begin{bmatrix} \mathrm{norm}(\boldsymbol{J_1}) \\ \mathrm{norm}(\boldsymbol{J_3}) \times \mathrm{norm}(\boldsymbol{J_1}) \\ \mathrm{norm}(\boldsymbol{J_3}) \end{bmatrix}, \boldsymbol{J_C}^* = \begin{bmatrix} \boldsymbol{J_1} \\ \boldsymbol{J_2} \\ \boldsymbol{J_3} \end{bmatrix}, \quad \boldsymbol{J_3} = \boldsymbol{J_1} \times \boldsymbol{J_2} \tag{10}$$

where $\boldsymbol{J_1}$ and $\boldsymbol{J_2}$ are respectively the first and second row vector of image Jacobian matrix $\boldsymbol{J_C}$, norm(·) represents normalization. Consequently, we have the rotation matrix for the rotary angle θ around the rotation axis f in $\{\boldsymbol{M}\}$ can be computed based on $\boldsymbol{f_{C'}}$ as follows.

$$\boldsymbol{R}(f_M, \theta) = \boldsymbol{J_{C'}}^* \boldsymbol{R}(f_{C'}, \theta)(\boldsymbol{J_C}^*)^{-1} = (\boldsymbol{J_{C'}}^* \boldsymbol{S}^*) \boldsymbol{R}(z, \theta)(\boldsymbol{J_{C'}}^* \boldsymbol{S}^*)^{-1} \tag{11}$$

where $\boldsymbol{S}^*$ is the rotation matrix which can transform $\{\boldsymbol{C'}\}$ to a new auxiliary coordinate system, aligning its w'-axis with the rotation axis f.

Next, we need to calibrate the direction of the rotation axis in $\{\boldsymbol{C'}\}$. To this end, it is necessary to identify at least three feature points along the optical axis within the SEM images. As illustrated in Fig. 5, two eigenvectors formed by these three points, with zero components along the optical axis in the image space $\{\boldsymbol{C}\}$. As a rotation is executed, feature vectors can be tracked to observe the changes induced by the rotation operation. Taking n tracked feature vectors, the vectors in $\{\boldsymbol{C'}\}$ can be calculated from vectors in $\{\boldsymbol{C}\}$ as:

$$\begin{bmatrix} \Delta u_i \\ \Delta v_i \\ 0 \end{bmatrix}_{C'} = \boldsymbol{J_{C'}}^* (\boldsymbol{J_C}^*)^{-1} \begin{bmatrix} \Delta u_i \\ \Delta v_i \\ 0 \end{bmatrix}_{C} \tag{12}$$

where $[\Delta u_i, \Delta v_i]^{\mathrm{T}}$ is the i^{th} vector of feature in $\{\boldsymbol{C'}\}$ or $\{\boldsymbol{C}\}$.

In terms of a vector $[\Delta u, \Delta v, 0]^{\mathrm{T}}$ in $\{\boldsymbol{C}\}$, the component of the corresponding vector on the w'-axis in $\{\boldsymbol{C'}\}$ is zero. Therefore, the feature vectors after rotation can be calculated as follows.

$$\boldsymbol{R}(f_{C'}, \theta) \begin{bmatrix} \Delta u \\ \Delta v \\ 0 \end{bmatrix}_{C'} = \boldsymbol{R}(f_{C'}, \theta) \boldsymbol{J_{C'}}^* (\boldsymbol{J_C}^*)^{-1} \begin{bmatrix} \Delta u \\ \Delta v \\ 0 \end{bmatrix}_{C} = \begin{bmatrix} \Delta u' \\ \Delta v' \\ \Delta w' \end{bmatrix}_{C'} \tag{13}$$

Focused on the upper two rows, the equation can be expressed as following.

$$\begin{bmatrix} f_x' f_x' v\theta + c\theta & f_y' f_x' v\theta - f_z' s\theta \\ f_x' f_y' v\theta + f_z' s\theta & f_y' f_y' v\theta + c\theta \end{bmatrix} \begin{bmatrix} \Delta u \\ \Delta v \end{bmatrix}_{C'} = \begin{bmatrix} \Delta u' \\ \Delta v' \end{bmatrix}_{C'} \tag{14}$$

Following several calibration trials, $\boldsymbol{f_{C'}} = [f_x', f_y', f_z']^{\mathrm{T}}$ can be determined as follows.

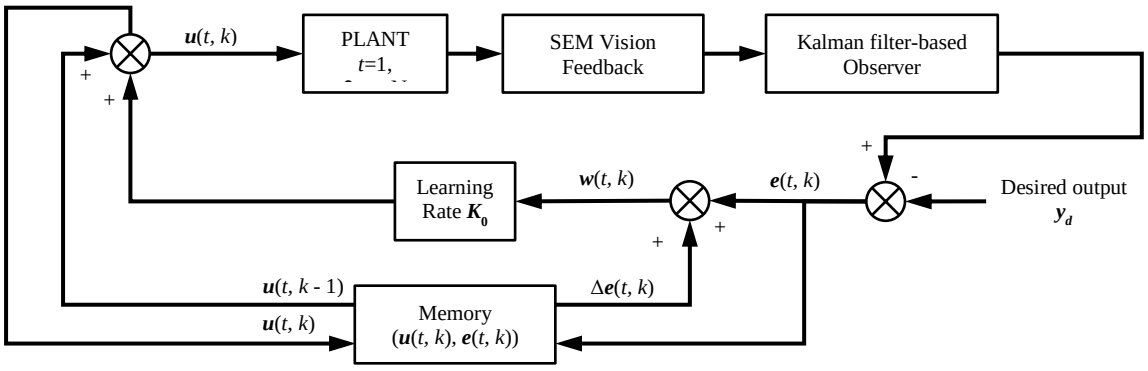

Fig. 6. Diagram of the proposed iterative learning control for in-situ rotating with Kalman filtering-based observer. The control input combines the previous input series and the high-order feedback regulation through Kalman filter-based observer and last iteration.

$$\begin{cases} |f_x'| = \sqrt{\dfrac{r_{11} - c\theta}{v\theta}}, |f_y'| = \sqrt{\dfrac{r_{22} - c\theta}{v\theta}}, |f_z'| = \dfrac{r_{21} - r_{12}}{2 \times s\theta} \\ \begin{bmatrix} r_{11} & r_{12} \\ r_{21} & r_{22} \end{bmatrix} = (\boldsymbol{X}_f{}^T \boldsymbol{X}_f)^{-1} \boldsymbol{X}_f{}^T \boldsymbol{Y}_f \\ \boldsymbol{X}_f = \begin{bmatrix} \Delta u_1 & \dots & \Delta u_n \\ \Delta v_1 & \dots & \Delta v_n \end{bmatrix}_{C'}, \boldsymbol{Y}_f = \begin{bmatrix} \Delta u_1' & \dots & \Delta u_n' \\ \Delta v_1' & \dots & \Delta v_n' \end{bmatrix}_{C'} \end{cases} \tag{15}$$

where n is the number of axis calibration trials. It's worth noting that the positiveness and negativeness of f_x', f_y' can be observed and judged from $(r_{21} + r_{12})$.

Final, the rotation axis in $\{\boldsymbol{M}\}$, denoted as $\boldsymbol{f_M}$, can be calculated using the following equation.

$$\boldsymbol{f_M} = (\boldsymbol{J}_{C'}^*)^{-1} \boldsymbol{f}_{C'} \tag{16}$$

And the rotation matrix about rotation angle θ over f in $\{\boldsymbol{M}\}$ can be calculated referring to (16) by known $[f_x', f_y', f_z']^T$ and rotation angle θ.

IV. High-order Iterative Learning Control with Kalman Filtering based Observer

Based on the kinematic model established earlier, achieving high-precision off-axis in-situ rotation still necessitates an efficient real-time compensation algorithm. In this section, we first introduce an iterative learning framework via full-state feedback and then elaborate on how full-state estimation is obtained through Kalman filtering. Finally, the paper briefly analyzes the stability of the overall system under the proposed control strategy which theoretically ensures the effectiveness of the proposed compensation algorithm for achieving high-precision off-axis in-situ rotation.

A. Iterative Learning Control (ILC)

Leveraging the repeatability of the rotational manipulation, the idea of iterative learning is employed to gradually reduce the offset between trajectory of the observed object (cantilever) and the desired position after each round of rotation, then ultimately achieving high-precision performance.

In virtue of the dynamic model (4), we propose the following ILC strategy.

$$\boldsymbol{u}(t, k+1) = \boldsymbol{u}(t, k) + \boldsymbol{K_0} \cdot \boldsymbol{w}(t, k+1) \tag{17}$$

where $\boldsymbol{u}(t, k)$ represents the compensation input series at the t^{th} step in the k^{th} iteration and $\boldsymbol{u}(t+1, k)$ the input signal at the $(t + 1)^{th}$ step in the k^{th} iteration. $\boldsymbol{K_0}$ is the learning rate parameter. $\boldsymbol{w}(t,k)$ is a proper defined full-state error signal reflecting the displacement of the observed object (cantilever) is at the t^{th} step in the k^{th} iteration, which is provided by the Kalman filter and discussed in the forthcoming subsections.

Unlike conventional iterative learning control [32], here, due to limited field of view (FoV) at high magnification under SEM, an arbitrary input for the first iteration cannot ensure the target object (cantilever) remain in SEM image. Thus, the initial input series are needed to be set properly. With the aid of calibration in Section III. *B*, the initial input series can be calculated as

$$\boldsymbol{u}(t,1) = (\boldsymbol{I} - \boldsymbol{R}(f, t \cdot \Delta\theta)) \cdot \boldsymbol{X_0} \tag{18}$$

where $\Delta\theta$ is the control step, $t \cdot \Delta\theta$ is the rotation angle at t^{th} step and $\boldsymbol{X_0}$ is set to be the pre-calibrated misalignment. This initial input compensation significantly constrains the displacement of the observed object.

B. Kalman Filter-based Observer

To facilitate the implementation of the proposed Iterative Learning Control (ILC) as outlined in equation (18), a crucial component is the full-state error signal $\boldsymbol{w}(t, k)$, which is contingent upon the precise spatial position of the observed object. Obtaining such a position is inherently challenging due to the limitations of SEM vision, which provides only 2D images, thus lacking depth information. Fortunately, as elucidated in Section II. *B*, it is observed that the trajectory of the observed object, specifically the cantilever, can be conceptualized as a composite of a circular path and subtle random perturbations, approximated as Gaussian noise. Consequently, the Kalman filter offers an effective and concise methodology for estimating the spatial position state by iteratively amalgamating predictions from the model and observations from SEM. The employed Kalman filter is

delineated as follows:

$$\text{predictor}\begin{cases}\hat{\boldsymbol{X}}_t^- = \boldsymbol{A}\hat{\boldsymbol{X}}_{t-1} + \boldsymbol{B}\boldsymbol{u}_t + \boldsymbol{E}\sum_{n=1}^{t-1}\boldsymbol{u}_n \\ \boldsymbol{P}_t^- = \boldsymbol{A}\boldsymbol{P}_{t-1}\boldsymbol{A}^T + \boldsymbol{Q}^*\end{cases} \tag{19}$$

$$\text{observation} \qquad \boldsymbol{Y}_t = \boldsymbol{C}\boldsymbol{X}_t \tag{20}$$

and

$$\text{corrector}\begin{cases}\boldsymbol{K}_t = \boldsymbol{P}_t^-\boldsymbol{C}^T(\boldsymbol{C}\boldsymbol{P}_t^-\boldsymbol{C}^T + \boldsymbol{R}^*)^{-1} \\ \hat{\boldsymbol{X}}_t = \hat{\boldsymbol{X}}_t^- + \boldsymbol{K}_t(\boldsymbol{Y}_t - \boldsymbol{C}\hat{\boldsymbol{X}}_t^-) \\ \boldsymbol{P}_t = (\boldsymbol{I} - \boldsymbol{K}_t\boldsymbol{C})\boldsymbol{P}_t^-\end{cases} \tag{21}$$

In (19)-(21), $\hat{\boldsymbol{X}}_{t-1}$ is the estimation of the spatial position of the observed object at time step k - 1, $\boldsymbol{u}_t$ is the input signal at the t^{th} step, as defined above in (18). Considering the kinematics model (4), we have parameter setting as

$$\boldsymbol{A} \equiv \boldsymbol{R}(f, \Delta\theta), \boldsymbol{B} \equiv \boldsymbol{I}_{3\times 3}, \boldsymbol{E} \equiv \boldsymbol{I} - \boldsymbol{R}(f, \Delta\theta), \boldsymbol{C} \equiv \boldsymbol{J}_C \tag{22}$$

The estimation $\hat{\boldsymbol{X}}_t^-$ of the spatial position of the observed object at time step t purely based on the kinematics model. The initial spatial position $\boldsymbol{X_0}$ is set to be the misalignment.

$\boldsymbol{Y_t}$ is the position on the image plane where the origin of the image plane is aligned to the origin of the coordinate system $\{\boldsymbol{E}\}$. Note, the observation $\boldsymbol{Y_t}$ cannot be extracted directly from SEM image since the origin of coordinate system $\{\boldsymbol{E}\}$ is unknown on image plane. Through relative displacement by the initial position, the observation $\boldsymbol{Y_t}$ can be calculated from SEM image as following

$$\boldsymbol{Y}_t = \boldsymbol{y}_t - \boldsymbol{y}_d + \boldsymbol{C}\cdot\boldsymbol{X}_0 \tag{23}$$

where $\boldsymbol{y_t}$ is the position on image plane at t^{th} step, $\boldsymbol{y_d}$ is the desired output as same as the initial position on image plane and $\boldsymbol{X_0}$ is the initial spatial position.

$\boldsymbol{Q}^*$ and $\boldsymbol{R}^*$ are the covariance matrices associated with the spatial position prediction and observation of the observed object (cantilever). As discussed in the preceding Section II. *B*, an examination of prediction noise revealed its independence along each axis. Consequently, $\boldsymbol{Q}^*$ in (19) and $\boldsymbol{R}^*$ in (21) can be configured as diagonal matrices. Considering the detection errors in the experiment, inherent image errors due to resolution limitations, and for simplicity, the values on the diagonal of $\boldsymbol{Q}^*$ are uniformly set to 1000000, while the values on the diagonal of $\boldsymbol{R}^*$ are all set to 1. This implies that estimated position relies more on observation, which helps avoid large variation between model and real trajectory. The initial value of the state estimation covariance matrix $\boldsymbol{P_0}$ is also set as a scaled identity diagonal matrix, with the values on the diagonal set to 100 for simplicity.

Finally, the estimation of the spatial position $\boldsymbol{X_k}$ of the observed object (cantilever) is obtained by a weighted combination of the prediction and observation. The estimation of spatial position through Kalman filter then facilitates the full-state feedback compensation.

C. High-order Feedback Control

As illustrated in Fig. 6, in each iteration (one revolution of cantilever), within each iteration corresponding to one revolution of the cantilever, the input series from the preceding iteration is referenced through the high-order feedback error signal $\boldsymbol{w}(t, k)$ as delineated below.

$$\boldsymbol{w}(t,k) = \underbrace{\boldsymbol{X}(t,k) - \boldsymbol{X}_0}_{\text{current displacement}} + \underbrace{\boldsymbol{X}(t+1,k-1) - \boldsymbol{X}(t,k-1)}_{\text{differential displacement in the previous iteration}} \tag{24}$$

The spatial states, such as $\boldsymbol{X}(t, k)$, are provided by the Kalman filter-based observer. Due to space limitations, the convergence of the observation error is not discussed here. Note that, in contrast to the conventional iterative learning control [32], here, $\boldsymbol{w}(t, k)$ not only concerns the displacement in the last iteration, but also accounts for the differential displacement on the current t^{th} step, which motivates the name of 'high-order feedback'. Note that in the first iteration, only the displacement on the current t^{th} step is considered. With the displacement signed as $\boldsymbol{e}(t, k)$, the expression of feedback term can be simplified as follows.

$$\boldsymbol{w}(t,k) = \boldsymbol{e}(t,k) + \Delta\boldsymbol{e}(t,k\text{-}1) \tag{25}$$

In summary, we proposed a Kalman filter-based high order ILC, where the iterative learning framework capitalizes on the inherent repeatability in rotation, complemented by the Kalman filtering-based observer, which facilitates state estimation through the integration of prediction and observation. This integration effectively minimizes disparities between the model and the actual trajectory, concurrently addressing random noise concerns. Within the context of high-order feedback design, the inclusion of both these displacements, encompassing their proportional and differential information from the preceding iteration during rotary motion, contributes to swift convergence and heightened precision within the designed controller. The efficacy of the proposed control methodology will be scrutinized, and comparative assessments will be conducted with alternative methods in the forthcoming experiments outlined in Section V.

D. Stability Analysis

To distinguish the estimation $\boldsymbol{X_t}$ in (21) and the true state in (4), in the following we rewrite the dynamic model (4) transforming as follows:

$$\begin{aligned}\boldsymbol{X}(t+1,k) &= \boldsymbol{A}\boldsymbol{X}(t,k) + \boldsymbol{B}\boldsymbol{u}(t,k) + \boldsymbol{E}\sum_{i=0}^{t-1}\boldsymbol{u}(i,k) + \boldsymbol{\delta}(t,k) \\ \boldsymbol{Y}(t+1,k) &= \boldsymbol{C}\boldsymbol{X}(t+1,k)\end{aligned} \tag{26}$$

where $\boldsymbol{B}$ is an identical matrix with appropriate dimensions. And $t \in \{0,1,2,...,N\}$, $k \in \{1,2,...,\infty\}$ for some positive integer N. The control objective is forcing $\boldsymbol{X}(t,k) \to \boldsymbol{X}_d(t)$ at each time instant. In this paper, we have $\boldsymbol{x}_d(t) = \boldsymbol{x}(0,1)$.

For (26), it can be rewritten as

$$\begin{aligned} \boldsymbol{X}(t+1,k) &= \boldsymbol{A}\boldsymbol{X}(t,k) + \boldsymbol{B}\boldsymbol{v}(t,k) + \boldsymbol{\delta}(t,k) \\ \boldsymbol{Y}(t+1,k) &= \boldsymbol{C}\boldsymbol{X}(t+1,k) \end{aligned} \tag{27}$$

where $\boldsymbol{v}(t,k) = \boldsymbol{u}(t,k) + \boldsymbol{E}\sum_{i=0}^{t-1}\boldsymbol{u}(i,k)$.

For system (28), we assume the following assumption holds, which is general in the ILC committee.

Assumption 1: There exists a unique bounded input sequence $\boldsymbol{v}_d(t)$ such that the system state $\boldsymbol{X}(t, k)$ follows $\boldsymbol{X}_d(t)$ with a prescribed accuracy ε as follows:

$$\forall t \in [0, N], \left\|\boldsymbol{X}(t,k) - \boldsymbol{X}_d(t)\right\| \le \varepsilon .$$

Assumption 2: The initial condition of (27) is known as calibration, i.e. $\boldsymbol{X}(0, k) = \boldsymbol{X}_d(0)$ for all $k \in \{1,2,...,\infty\}$.

Assumption 3: External disturbance $\boldsymbol{\delta}(t, k)$ is nonrepetitive, but the variations of $\boldsymbol{\delta}(t, k)$ with respect to the iteration k are bounded with a positive constant δ_f, i.e.

$$\left\|\boldsymbol{\delta}(t,k+1) - \boldsymbol{\delta}(t,k)\right\| \le \delta_f$$

The control law is given as

$$\begin{aligned} \boldsymbol{v}(t,k+1) &= \boldsymbol{v}(t,k) + \boldsymbol{K}_0\boldsymbol{w}(t,k+1) \\ \boldsymbol{e}(t,k+1) &= \boldsymbol{X}(t,k+1) - \boldsymbol{X}_d(t) + \boldsymbol{X}(t+1,k) - \boldsymbol{X}(t,k) \end{aligned} \tag{28}$$

To facilitate subsequent analysis, we apply a time shift to $\boldsymbol{X}_d(t)$, i.e. $\boldsymbol{X}_d(t)$ in (28) is replaced by $\boldsymbol{X}_d(t + 1)$. This operation is reasonable, as $\boldsymbol{X}_d(t)$ exhibits a constant nature in this article. Then, the control law (28) can be rewritten as

$$\begin{aligned} \boldsymbol{v}(t,k) &= \bar{\boldsymbol{v}}(t,k) + \boldsymbol{K}_0 X(t,k) \\ \bar{\boldsymbol{v}}(t,k+1) &= \bar{\boldsymbol{v}}(t,k) + \boldsymbol{K}_0(X(t+1,k) - \boldsymbol{X}_d(t+1)) \end{aligned} \tag{29}$$

Now, we can rewrite the system (27) and control law (29) as

$$\begin{aligned} \boldsymbol{x}(t+1,k) &= \bar{\boldsymbol{A}}\boldsymbol{X}(t,k) + \boldsymbol{B}\bar{\boldsymbol{v}}(t,k) + \boldsymbol{\delta}(t,k) \\ \boldsymbol{y}(t+1,k) &= \boldsymbol{C}\boldsymbol{X}(t+1,k) \\ \bar{\boldsymbol{v}}(t,k+1) &= \bar{\boldsymbol{v}}(t,k) + \boldsymbol{K}_0(\boldsymbol{X}(t+1,k) - \boldsymbol{X}_d(t+1)) \end{aligned} \tag{30}$$

where $\bar{\boldsymbol{A}} = \boldsymbol{A} + \boldsymbol{B}\boldsymbol{K}_0$.

Define the tracking error on iteration k as

$$\boldsymbol{e}(t,k) = \boldsymbol{X}(t,k) - \boldsymbol{X}_d(t)$$

In addition, we use $\boldsymbol{z}(t,k) = \boldsymbol{X}(t+1,k)$, then we have the $\boldsymbol{e}_z(t,k) = \boldsymbol{X}(t+1,k) - \boldsymbol{X}_d(t+1)$, the control law thereby becomes $\bar{\boldsymbol{v}}(t,k+1) = \bar{\boldsymbol{v}}(t,k) + \boldsymbol{K}_0\boldsymbol{e}_z(t,k)$.

Let

$$\boldsymbol{Z}(k) = \begin{bmatrix} \boldsymbol{X}(1,k) \\ \boldsymbol{X}(2,k) \\ \vdots \\ \boldsymbol{X}(N,k) \end{bmatrix}, \boldsymbol{U}(k) = \begin{bmatrix} \bar{\boldsymbol{v}}(0,k) \\ \bar{\boldsymbol{v}}(1,k) \\ \vdots \\ \bar{\boldsymbol{v}}(N-1,k) \end{bmatrix},$$

$$\boldsymbol{Z}_d = \begin{bmatrix} \boldsymbol{X}_d(1) \\ \boldsymbol{X}_d(2) \\ \vdots \\ \boldsymbol{X}_d(N) \end{bmatrix}, \boldsymbol{F}(k) = \begin{bmatrix} \boldsymbol{\delta}(0,k) \\ \boldsymbol{\delta}(1,k) \\ \vdots \\ \boldsymbol{\delta}(N-1,k) \end{bmatrix}$$

Based on the lifted-vector-matrix technique above, system (30) can be reformulated as an input-output transmission form described by

$$\boldsymbol{Z}(k) = \boldsymbol{H}\boldsymbol{U}(k) + \boldsymbol{\phi}\boldsymbol{F}(k) \tag{31}$$

$$\boldsymbol{U}(k+1) = \boldsymbol{U}(k) + \boldsymbol{K}_0\boldsymbol{E}_z(k) \tag{32}$$

$$\boldsymbol{E}_z(k) = \boldsymbol{Z}(k) - \boldsymbol{Z}_d \tag{33}$$

where we have

$$\boldsymbol{H} = \begin{bmatrix} \boldsymbol{B} & \boldsymbol{0} & \cdots & \boldsymbol{0} \\ \bar{\boldsymbol{A}}\boldsymbol{B} & \boldsymbol{B} & \ddots & \vdots \\ \vdots & \ddots & \ddots & \boldsymbol{0} \\ \bar{\boldsymbol{A}}^{N-1}\boldsymbol{B} & \cdots & \boldsymbol{A}\boldsymbol{B} & \boldsymbol{B} \end{bmatrix}, \boldsymbol{\phi} = \begin{bmatrix} \boldsymbol{I} & \boldsymbol{0} & \cdots & \boldsymbol{0} \\ \bar{\boldsymbol{A}} & \boldsymbol{I} & \ddots & \vdots \\ \vdots & \ddots & \ddots & \boldsymbol{0} \\ \bar{\boldsymbol{A}}^{N-1} & \cdots & \bar{\boldsymbol{A}} & \boldsymbol{I} \end{bmatrix}$$

In this article, the following lemmas are introduced before the main result is presented.

Lemma 1.1: [1] For a matrix $\boldsymbol{P} \in \mathbb{R}^{n\times n}$, there must exist a matrix norm $\|\cdot\|$ such that

$$\|\boldsymbol{P}\| \le \rho(\boldsymbol{P}) + \kappa$$

where $\forall \kappa > 0$, $\rho(\boldsymbol{P})$ is the spectral radius of matrix $\boldsymbol{P}$.

Proof: According to the Jordan decomposition theorem, there exists an invertible matrix $\boldsymbol{Q}$, such that

$$\boldsymbol{Q}^{-1}\boldsymbol{P}\boldsymbol{Q} = \begin{pmatrix} \lambda_1 & \psi_1 & 0 & \cdots & 0 & 0 \\ 0 & \lambda_2 & \psi_2 & \cdots & 0 & 0 \\ \cdots & \cdots & \cdots & \cdots & \cdots & \cdots \\ 0 & 0 & 0 & \cdots & \lambda_{n-1} & \psi_{n-1} \\ 0 & 0 & 0 & \cdots & 0 & \lambda_n \end{pmatrix}$$

where $\lambda_i (i = 1, 2, 3, \ldots, n)$ are the eigenvalues of matrix P and $\psi_j = 1$ or 0, $j = 1, 2, \ldots, n - 1$. Let $D = \mathrm{diag}(1, \kappa, \kappa^2, \ldots, \kappa^{n-1})$, and one has

$$\boldsymbol{D}^{-1}\boldsymbol{Q}^{-1}\boldsymbol{P}\boldsymbol{Q}\boldsymbol{D} == \begin{pmatrix} \lambda_1 & \kappa\psi_1 & 0 & \cdots & 0 & 0 \\ 0 & \lambda_2 & \kappa\psi_2 & \cdots & 0 & 0 \\ \cdots & \cdots & \cdots & \cdots & \cdots & \cdots \\ 0 & 0 & 0 & \cdots & \lambda_{n-1} & \kappa\psi_{n-1} \\ 0 & 0 & 0 & \cdots & 0 & \lambda_n \end{pmatrix}$$

Then, define the matrix norm

$$\|\boldsymbol{P}\| = \left\|\boldsymbol{D}^{-1}\boldsymbol{Q}^{-1}\boldsymbol{P}\boldsymbol{Q}\boldsymbol{D}\right\|_\infty \tag{34}$$

One can get $\left\|\boldsymbol{D}^{-1}\boldsymbol{Q}^{-1}\boldsymbol{P}\boldsymbol{Q}\boldsymbol{D}\right\|_\infty \le \max_i(|\lambda_i| + \kappa) = \rho(\boldsymbol{P}) + \kappa$.

Lemma 1.2: [1] For a matrix $\boldsymbol{P} \in \mathbb{R}^{n\times n}$, a vector $\boldsymbol{X} \in \mathbb{R}^n$, and an arbitrary matrix norm $\|\cdot\|$, there exists a vector norm $\|\cdot\|_*$ such that

$$\|\boldsymbol{P}\boldsymbol{X}\|_* \le \|\boldsymbol{P}\|\|\boldsymbol{X}\|_*$$

Proof: For any vector $\chi \ne 0 \in \mathbb{R}^n$, define the vector norm

$$\|\boldsymbol{X}\|_* = \left\|\boldsymbol{X}\chi^{\mathrm{T}}\right\|$$

where $\|\cdot\|$ is the matrix norm in (36). Then, one have

TABLE I. EXPERIMENTAL RESULTS ON OFF-AXIS ROTATING CONTROL METHODS

Exp. No.	Control method	Magnification	Step angle	Round No.	Average position shift	Maximum position shift	Standard deviation
			$\Delta\theta$(°)	/	S_{avg} (nm)	S_{max} (nm)	SD (nm)
1	None	/	1	/	417058	866532	311389
2	PID	1000	1	/	3462	24609	2926
3	MPC	1000	1	/	4466	41208	5545
4	Ours	500	1	1	2399	19204	2426
				4	1924	11893	1691
5		1000	0.5	1	1700	47620	2765
				5	1441	11016	**1336**
6			1	1	2149	13002	1916
				4	**1374**	**10050**	1386
7			5	1	7466	22444	4904
				4	3635	17418	2622
8		2000	1	1	2236	12207	1943
				2	1921	15021	1818

$$\|\boldsymbol{PX}\|_* = \|\boldsymbol{PX\chi}^{\mathrm{T}}\|_* \le \|\boldsymbol{P}\| \cdot \|\boldsymbol{X\chi}^{\mathrm{T}}\| = \|\boldsymbol{P}\| \cdot \|\boldsymbol{X}\|_*$$

From (34), we have

$$\begin{aligned}\boldsymbol{E}_z(k+1) &= \boldsymbol{Z}(k+1) - \boldsymbol{Z}_d \\ &= \boldsymbol{HU}(k+1) + \boldsymbol{\phi F}(k+1) - \boldsymbol{Z}_d \\ &= \boldsymbol{HU}(k+1) + \boldsymbol{\phi F}(k+1) + \boldsymbol{E}_z(k) - \boldsymbol{Z}(k)\end{aligned}$$

In view of (33), one can obtain that

$$\begin{aligned}\boldsymbol{E}_z(k+1) &= \boldsymbol{H}[\boldsymbol{U}(k) + \boldsymbol{K}_0\boldsymbol{E}_z(k)] + \boldsymbol{\phi F}(k+1) + \boldsymbol{E}_z(k) \\ &\quad -[\boldsymbol{HU}(k) + \boldsymbol{\phi F}(k)] \\ &= (\boldsymbol{I} + \boldsymbol{HK}_0)\boldsymbol{E}_z(k) + \boldsymbol{\phi}\delta\boldsymbol{F}(k) \\ &= \boldsymbol{LE}_z(k) + \boldsymbol{\phi}\delta\boldsymbol{F}(k)\end{aligned}$$

where $\delta\boldsymbol{F}(k) = \boldsymbol{F}(k+1) - \boldsymbol{F}(k)$, and

$$\boldsymbol{L} = \begin{bmatrix} \boldsymbol{I} + \boldsymbol{BK}_0 & \boldsymbol{0} & \cdots & \boldsymbol{0} \\ \bar{\boldsymbol{A}}\boldsymbol{B} & \boldsymbol{I} + \boldsymbol{BK}_0 & \ddots & \vdots \\ \vdots & \ddots & \ddots & \boldsymbol{0} \\ \bar{\boldsymbol{A}}^{N-1}\boldsymbol{B} & \cdots & \bar{\boldsymbol{A}}\boldsymbol{B} & \boldsymbol{I} + \boldsymbol{BK}_0 \end{bmatrix}$$

From Assumption 3, there must exist positive constants η_F satisfying the inequality

$$\|\boldsymbol{\phi}\delta\boldsymbol{F}(k)\|_* \le \eta_F$$

Together with the fact that, for a lower triangular matrix $\boldsymbol{P} \in \mathbb{R}^{n\times n}$, we have $\|\boldsymbol{P}^k\| \le \|\boldsymbol{P}\|^k$. By using Lemma 1.2, we have

$$\begin{aligned}\|\boldsymbol{E}_z(k+1)\|_* &\le \|\boldsymbol{L}^{k+1}\|\|\boldsymbol{E}_z(0)\|_* + \sum_{i=0}^{k}\|\boldsymbol{L}\|^{k-i}\eta_F \\ &\le \|\boldsymbol{L}\|^{k+1}\|\boldsymbol{E}_z(0)\|_* + \frac{1\cdot(1-\|\boldsymbol{L}\|^{k+1})}{1-\|\boldsymbol{L}\|}\eta_F\end{aligned}$$

Then, together with the fact that $\|\boldsymbol{E}_z(0)\|$ is bounded, we have

$$\lim_{k\to\infty}\|\boldsymbol{E}_z(k+1)\|_* \le \lim_{k\to\infty}\|\boldsymbol{L}\|^{k+1}\|\boldsymbol{E}_z(0)\|_* + \frac{1}{1-\|\boldsymbol{L}\|}\eta_F$$

Consider Lemma 1.1, we know, if the selection of K_0 satisfies the condition $0 < \beta = \rho(\boldsymbol{I} + \boldsymbol{BK}_0) + \kappa < 1$ for $\kappa > 0$, then we have $\|\boldsymbol{E}_z(k+1)\|_* \le \eta_F / (1-\|\boldsymbol{L}\|)$. Therefore, the tracking error between $\boldsymbol{X}(t)$ and $\boldsymbol{X_d}(t)$ will converge to a neighborhood of the origin, together with the Assumption 2.

Remark 1: From the analysis process, the convergence performance of the algorithm we propose is only related to the magnitude of external disturbances varying with iterations. The smaller the magnitude, the higher the convergence accuracy. This means that even if the in-situ control system is subjected to significant external disturbances, as long as these disturbances is repetitive with respect to the iteration number, our algorithm can keep probe stationary in its initial position.

V. EXPERIMENT AND RESULTS

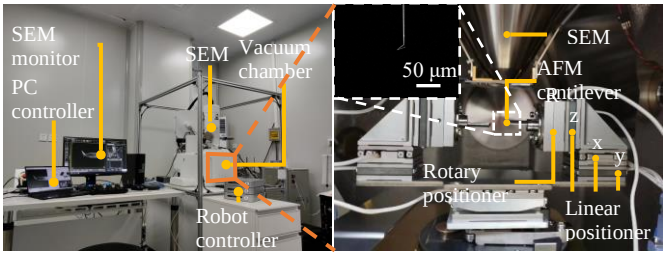

Fig. 7. Experimental nano-manipulation platform equipped with ECSx3030, ECR3030 nanopositioners (Attocube Systems AG), and JEOL JSM-IT500HR/LA InTouchScope™ SEM. AFM cantilever is used as robot end-effector for in-situ point rotating control validation.

This section validates, through experiments, the capability of the proposed nanorobotic manipulation system, in conjunction with the high-order iterative learning control algorithm based on Kalman filtering, to achieve high-precision off-axis in-situ rotation. Additionally, a comparative analysis is conducted with PID controllers and model predictive control (MPC) to underscore the superior performance of the proposed method.

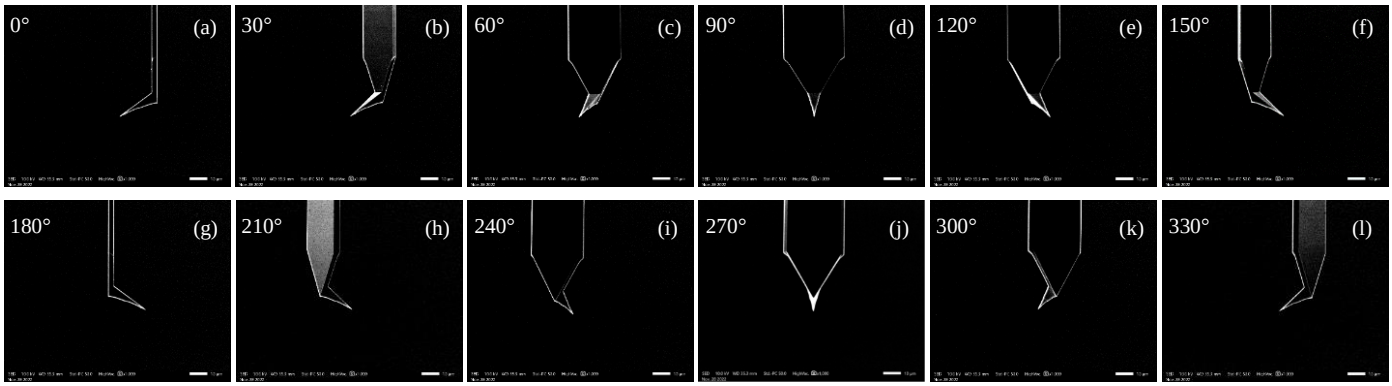

Fig. 8. SEM images of a cantilever's in-situ rotating experiment with rotation range of 360° and rotation step size of 1°. (a) θ = 0°. (b) θ = 30°. (c) θ = 60°. (d) θ = 90°. (e) θ = 120°. (f) θ = 150°. (g) θ = 180°. (h) θ = 210°. (i) θ = 240°. (j) θ = 270°. (k) θ = 300°. (l) θ = 330°. The magnification is 1000 and the length of scale bar is 10 μm. The AFM cantilver used here is NANOSENSORS ATEC-FM.

A. Experimental Setup

Fig. 7 displays the established nanorobotic manipulation system. The scanning electron microscope used in this system is JEOL JSM-IT500HR/LA, operating in high vacuum mode to image samples by detecting secondary electrons, under 10 KV acceleration voltage, which captures 7 frames per second (frame/s) with image size of 640 × 480. The cantilever employed in this experiment was NANOSENSORS ATEC-FM. The translational nanopositioners, which are orthogonally mounted in this nanorobotic manipulation system, were Attocube piezoelectric ECSx3030, representing *x*-, *y*-, *z*-axes. The rotational nanopositioner is an Attocube piezoelectric ECR3030, with the rotation axis situated close to *y*-axis in $\{\boldsymbol{M}\}$. The translational positioners offer repeatability precision of 50 nm.

B. Evaluation Metric

To properly assess the performance of the rotary manipulation, we utilize the positional shift of i^{th} step, denoted as $SFT(i)$, obtained from the SEM images and calculate the average position shift SFT_{avg}, during the entire rotating process as follows:

$$SFT(i) = \left\| \boldsymbol{J_C}^{-1} \left(\begin{bmatrix} u_P(i) \\ v_P(i) \\ 0 \end{bmatrix} - \begin{bmatrix} u_{target} \\ v_{target} \\ 0 \end{bmatrix} \right) \right\|_2 , \; SFT_{avg} = \frac{1}{T} \sum_{i=1}^{T} SFT(i) \tag{35}$$

where $\boldsymbol{J_C}$ is the image Jacobian matrix at the current magnification for transformation from 3D motion space $\{\boldsymbol{M}\}$ to *u*-*v* image plane in $\{\boldsymbol{C}\}$. The coordinates $u_P(i)$ and $v_P(i)$ represent the coordinates along the *u*-axis and *v*-axis, respectively, of the point projected onto the image plane at the i^{th} instant for a given feature point. Similarly, u_{target} and v_{target} denote the coordinates along the *u*-axis and *v*-axis, respectively, corresponding to the projection of the initial values (initially positioned rotational target values) onto the image plane.

In addition to the average position shift, we also define the maximum position shift SFT_{max}, and the standard deviation of position (SD) throughout the entire rotating process as below:

$$SFT_{max} = \max_{1 \le i \le n} \{SFT(i)\} \tag{36}$$

$$SD = \sqrt{\frac{1}{n-1} \sum_{i=1}^{n} (SFT(i) - SFT_{avg})} \tag{37}$$

The image Jacobian matrix is computed based on the calibrated Jacobian matrix and the applied magnification [35]. Specifically, for the experiments conducted in this study at a magnification of 1000, the image Jacobian matrix is established as follows:

$$\boldsymbol{J_C} = \begin{bmatrix} 2.20e-4 & 5.07e-3 & -6.25e-5 \\ 5.11e-3 & -8.66e-5 & -5.00e-6 \\ -3.08e-8 & -3.18e-7 & -2.59e-5 \end{bmatrix} \text{ pixel/nm}$$

To calibrate the initial misalignment, we implement the methodology detailed in Section III.B through four movement trials involving a rotation of 15°, This process yields the initial misalignment vector $[\Delta x_f, \Delta y_f, \Delta z_f]^{\text{T}}$ = [396123, 0, 214680]$^{\text{T}}$ nm. Subsequently, employing the approach outlined in Section III.C, we capture two images before and after a rotation angle of 60° to calibrate the rotation axis. The outcome of this calibration procedure estimates the rotation axis, denoted as vector $\boldsymbol{f_M}$, as [0.098, -0.9999, 0.0098]$^{\text{T}}$. Regarding observer, the values on the diagonal of $\boldsymbol{Q}^*$ are uniformly set to 1000000, while the values on the diagonal of $\boldsymbol{R}^*$ are all set to 1.

C. Off-Axis In-situ Rotation

The primary objective of off-axis in-situ rotation is to maintain the target point, situated at the tip of the AFM cantilever, in-situ through rotational manipulation. The SEM images in this experiment with tip rotation of 360° and step size of 1° are shown in Fig. 8. The tip's position is monitored through edge point detection using the Canny operator, implemented with a strong threshold of 150 and a weak threshold of 250. Initially, it is noted that the tip displays an offset of about 451 μm from the rotation axis. This value is considerably larger than the field of view at a magnification of, for example, 1000, which is constrained to 128 μm. Additionally, the rotation axis is observed to closely align with the *y*-axis in $\{\boldsymbol{M}\}$, signifying that the offset is more pronounced along the u-axis in the image space $\{\boldsymbol{C}\}$.

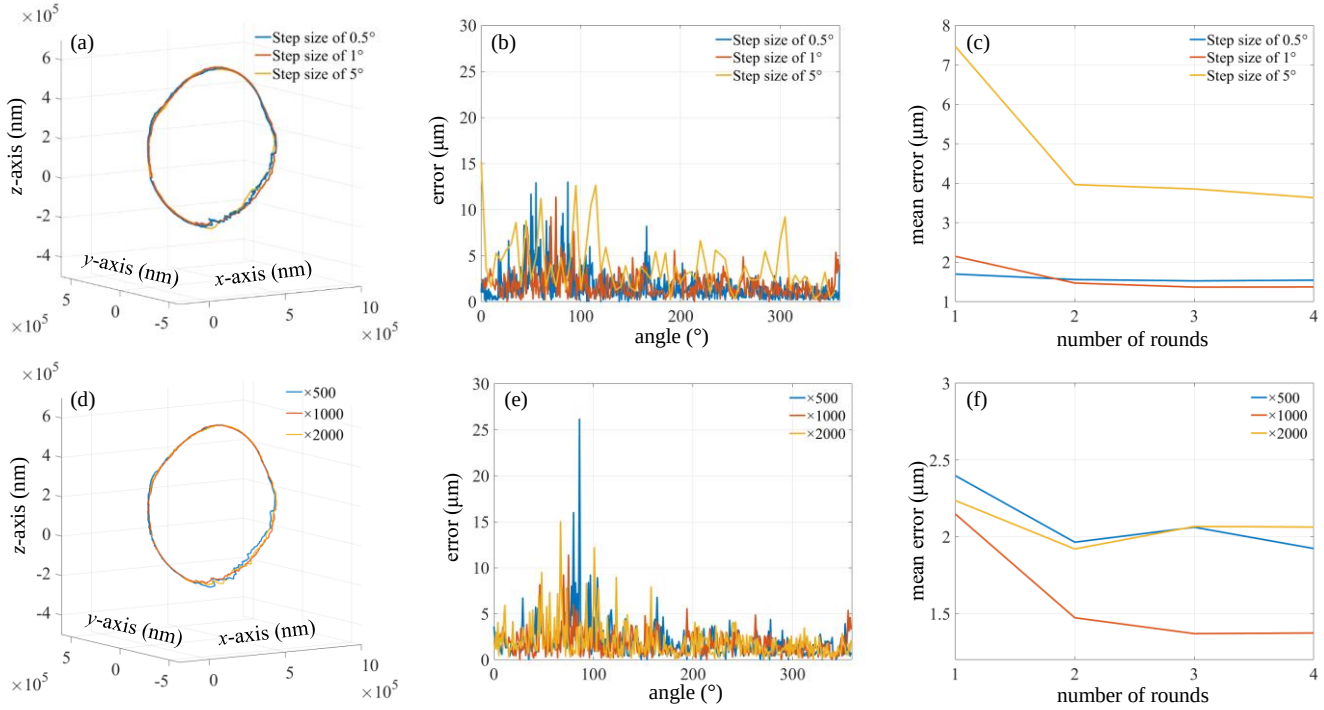

Fig. 9. Rotating experimental results at different magnifications and step sizes. (a)-(c) Real path of linear nano-positioners' compensation, position error of point of interest on image plane, and trend of average position error with increase of rounds under different step sizes. (d)-(f) Real path of linear nano-positioners, position error on image plane, and trend of average position error with increase of rounds under different magnifications.

To validate the efficiency of our system under various working magnifications while considering different manipulation requirements, experiments employing the proposed high-order ILC method were conducted at different control step sizes and magnifications. Specifically, the SEM magnification was set at 500, 1000, and 2000. Three distinct step sizes, namely 0.5°, 1°, and 5°, were selected. But the learning rate, denoted as $\boldsymbol{K_0}$, was consistently set to diag{-0.9, -0.9, -0.9} for all experiments.

The visual results of some representative experiments are depicted in Fig. 9. Specifically, Fig. 9(a)-(c) illustrate the real trajectory of the robot, the positioning error of the second tip, and the average positional deviation across different iterations in three off-axis in-situ rotation experiments with step sizes of 0.5°, 1°, and 5°, and a magnification of 1000. It is evident that larger step sizes result in greater positional errors with each rotation, leading to increased oscillations in the trajectory. Nevertheless, under all three step sizes, the algorithm demonstrates convergence, and the proposed control method performs well, particularly with step sizes of 0.5° and 1°, where the average positional deviation is notably low. With a step size of 1°, Fig 9(d)-(f) demonstrates the effect of magnifications of 500, 1000, and 2000 on the performance of rotational manipulation. As illustrated, a magnification of 500 introduces larger positional errors and higher oscillations. However, a larger magnification does not necessarily always yield better results, as evident in Fig. 9(f).

Table I enumerates further quantitative performance metrics of in-situ rotation, encompassing average position shift, maximum shift, and standard deviation. Fig. 9, in conjunction with Table I, collectively corroborates the effectiveness of the proposed off-axis in-situ rotation control method across varying magnification factors and rotation step sizes, maintaining the target point close to its original position. Moreover, with an increasing number of iterative rotations, the ILC converges, thus the target point progressively approaches its original position in terms of the mean value. Overall, the proposed method demonstrates rapid convergence and stability in multiple iterations. It exhibits more precise performance, particularly at smaller step sizes. The method achieves optimal results in experiments conducted at a magnification factor of 1000x and a step size of 1°. In this scenario, the average position shift decreases significantly, from 417.058 μm to 1.374 μm, representing a remarkable 99.671% improvement in in-situ rotation accuracy.

D. Comparative Experiments

To further underscore the superiority of the proposed method, based on the same modeling framework as outlined in Section III. *A*, we conducted comparative analyses with widely-recognized control methods, specifically PID control, and Model Predictive Control (MPC). Experimental parameters for the comparative methods align with those specified in Section V.C with magnification of 1000 and step size of 1°. For the PID controller, the proportional gain K_P is set to 0.8, and the derivative gain K_D is set to 0.1. In the case of the MPC method, both the state and terminal state weighting matrices are configured as diag{2, 2, 2}, while the input weighting matrix is empirically determined as diag{10, 10, 10}.

The comparative results of the three methods are illustrated in Fig. 10 and in Table I. From Fig. 10(a), it is evident that the proposed method yields a smoother trajectory and smaller positional offsets. An empirical explanation to this fact is that

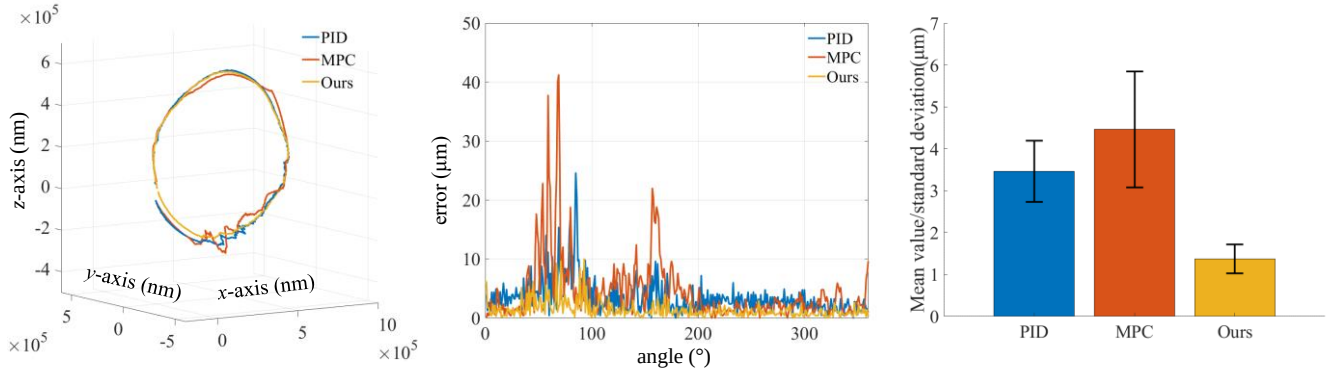

(a) (b) (c)

Fig. 10. Comparative experiment results over control strategy with PID controller and MPC. (a) Real paths for linear nano-positioners' compensation on tip motion displacement with PID, MPC and the proposed method. (b) Comparison on position error of point of interest on image plane. (c) Comparative results of mean value and standard deviation over position error.

when compared to the proposed method, both PID and MPC are more prone to deviating from the limited field of view. This tendency arises because PID is model-free, while MPC relies on the accuracy of the model. The method proposed in this study effectively balances these aspects, demonstrating a commendable utilization of prior knowledge and successful learning of properties related to the mechanical misalignment. The average values and standard deviations of the proposed method and the comparative methods are depicted in Fig. 10(c) and Table I, reflecting the superior precision of the proposed method for the off-axis in-situ rotation under SEM.

E. Discussion

The superiority of the off-axis in-situ rotation control method proposed in this paper is primarily manifested in the following aspects: Firstly, unlike linear motion, the rotation of a nanorobotics device generates significant spatial misalignment while undergoing precise attitude transformations. The prevailing approach to address this involves aligning the end effector to have the tracking point centered around the axis of rotation. However, these methods demand strict hardware configurations and the use of two nanometer positioning devices. In this paper, we position a rotary nano-positioner mounted at the end joint and employ the proposed method to maintain the target point in-situ during the off-axis rotational manipulation. Consequently, the nanorobotic manipulation system imposes no restrictions on the direction of the rotation axis, thereby relaxing system configurations. Secondly, the proposed control method fully leverages the repeatability of in-situ rotation, demonstrating iterative learning capabilities and an asymptotically converged precision in is-situ rotation. Specifically, our method restricts the average displacement of the target point from the in-situ position to 1.374 μm. In comparison, without compensation, the average displacement of the target point is 417.059 μm. Using a PID controller, only a reduction to 3.462 μm in average position deviation is achievable, while employing the MPC method results in a reduction to 4.466 μm. Similarly, our method outperforms others in terms of maximum position deviation and standard deviation during in-situ rotation (see Table I). Finally, our method exhibits excellent stability under different step sizes and SEM magnification settings. Some empirical insight on the relation between specific configurations and the precision in in-situ rotation is given as follows. In comparative rotation experiments with different step sizes, the positional deviation at a 1° step size is less than that at a 5° step size, attributed to the immediate feedback provided by the smaller step size. However, due to uncontrollable random mechanical noise, the performance at a 0.5° step size is slightly inferior to that at a 1° step size. In rotation experiments at different magnification settings, the positional error at a 500x magnification is less than that at a 1000x magnification. This difference can be attributed to the higher resolution images provided by SEM at a 500x magnification, with an approximately 200 nm/pixel resolution. On the other hand, the performance at a magnification of 2000x is poorer than that at 1000x, as the Jacobian matrix at a magnification of 2000x is estimated based on the Jacobian matrix at a magnification of 1000x, leading to larger observation errors in the Kalman filter.

VI. Conclusion

This paper establishes an advanced nanorobotic system and its control methodology, achieving precise off-axis in-situ rotation within a SEM with an average deviation of less than 1.374 μm. This result represents a significant improvement of 99.671% compared to the uncompensated condition. Initially, the nanorobotic manipulation system is constructed by utilizing a nanometer rotatory positioner as an end joint. Subsequently, we model the system and provide a calibration method that does not require alignment with the central axis and rotation axis. Calibration is accomplished with a single view, consistent with the visual feedback settings during the final rotation operation. Lastly, based on the established model, we propose an iterative learning control method using the Kalman filter and conduct the stability analysis and convergence proof. Through carefully designed experiments, we validate the stability, reliability, and performance of the proposed technique. This off-axis rotation control strategy can be seamlessly applied to other nanorobotic manipulation

systems, relaxing the need for linear degrees of freedom specifically dedicated to centering. This has implications for various research applications, including defect detection in nanomaterials, 3D nanoscale observation, and characterization of nanomaterial distortions.

REFERENCES

[1] Y. Shen, M. Nakajima, Z. Zhang and T. Fukuda, "Dynamic Force Characterization Microscopy Based on Integrated Nanorobotic AFM and SEM System for Detachment Process Study," in *IEEE/ASME Transactions on Mechatronics*, vol. 20, no. 6, pp. 3009-3017, Dec. 2015.

[2] P. Gao, J. Gao, T. Zou, and W. Rong, "The Measurement of the Elastic Modulus and Kinetic Friction Coefficient of Long Nanowires by the Micro-force Probe in the SEM Combined with Finite Element Simulation," *IEEE International Conference on Nanoscience and Technology*, pp. 58-63, 2021.

[3] Huiyang Ding, Li Ma, "Visual Servoing-Based Nanorobotic System for Automated Electrical Characterization of Nanotubes inside SEM" *Sensors*, vol. 18, no. 4, pp. 1137, 2018.

[4] J. Qu et al., "An SEM-Based Nanomanipulation System for Multiphysical Characterization of Single InGaN/GaN Nanowires," in *IEEE Transactions on Automation Science and Engineering*, doi: 10.1109.

[5] Shen, Feiling, et al. "Structure characterization of interior invisible single grain boundary by nanorobot pick-and-place grain in bulk ZnO under SEM." *Materials Letters* 324 (2022): 132777.

[6] Yang, Quan, et al. "Electrical Conductivity of Multiwall Carbon Nanotube Bundles Contacting with Metal Electrodes by Nano Manipulators inside SEM." *Nanomaterials* 11.5 (2021): 1290.

[7] P. Wang, H. Lu and Y. Shen, "Flexible 3-D Helix Fabrication by In-Situ SEM Micromanipulation System," in *IEEE Transactions on Industrial Electronics*, vol. 67, no. 7, pp. 5565-5574, July 2020.

[8] S. Zhuang, C. Dai, G. Shan, C. Ru, Z. Zhang and Y. Sun, "Robotic Rotational Positioning of End-Effectors for Micromanipulation," in *IEEE Transactions on Robotics*, vol. 38, no. 4, pp. 2251-2261, Aug. 2022.

[9] Cui, Tianyu, et al. "Single-cell level investigation of microbiologically induced degradation of passive film of stainless steel via FIB-SEM/TEM and multi-mode AFM." *Corrosion Science* 206 (2022): 110543.

[10] W. Shang, H. Lu, Y. Yang and Y. Shen, "7-DoFs Rotation-Thrust Microrobotic Control for Low-Invasive Cell Pierce via Impedance Compensation," in *IEEE/ASME Transactions on Mechatronics*, vol. 27, no. 6, pp. 5095-5106, Dec. 2022.

[11] A.A.G. Requicha, "Nanorobots, NEMS and Nanoassembly," *Proceedings of the IEEE*, vol. 91, no. 11, pp. 1922–1933, 2003.

[12] T. Fujiwara, M. Nakajima, A. Ichikawa, K. Ohara, Y. Hasegawa and T. Fukuda, "Bending of multi-graphene by nanomanipulation assisted with electron beam irradiation for box structure," *IECON 2015 - 41st Annual Conference of the IEEE Industrial Electronics Society*, 2015, pp. 002578-002583.

[13] M. Nakajima, M. Takeuchi, T. Fukuda, Y. Hasegawa and Q. Huang, "In situ nanomanipulation with 3D SEM-CT observation inside environmental SEM," *2015 International Symposium on Micro-NanoMechatronics and Human Science (MHS)*, 2015, pp. 1-2.

[14] W. Wan, H. Lu and Y. Shen, "Rotational nanorobotic manipulation system with increment alignment method for multi-directional defect characterization inside SEM," *IEEE/RSJ International Conference on Intelligent Robots and Systems*, 2017, pp. 1901-1906.

[15] Lu, Haojian, et al. "Nanorobotic system iTRo for controllable 1D micro/nano material twisting test." *Scientific reports* 7.1 (2017): 1-11.

[16] H. Lu, F. Xue, W. Wan and Y. Shen, "Investigation of Scaling Effect of Copper Microwire Based on in-Situ Nanorobotic Twisting Inside SEM," *IEEE International Conference on Robotics and Automation (ICRA)*, 2018, pp. 3461-3466.

[17] C. Han, L. Zhang, and Z. Yang, "Division of CNT placement meta-task for micro-nano robotic manipulator," *IEEE International Conference on Manipulation, Manufacturing and Measurement on the Nanoscale*, pp. 71-76, 2021.

[18] N. Marturi, B. Tamadazte, S. Dembélé, and N. Piat, "Visual Servoing-Based Depth-Estimation Technique for Manipulation Inside SEM," *IEEE Transactions on Instrumentation and Measurement*, vol. 65, no. 8, pp. 1847-1855, 2016.

[19] T. Kasaya, H. Miyazaki, S. Saito and T. Sato, "Micro object handling under SEM by vision-based automatic control," *Proceedings 1999 IEEE International Conference on Robotics and Automation (Cat. No.99CH36288C)*, 1999, pp. 2189-2196 vol.3.

[20] Y. Shen, W. Wan, H. Lu, T. Fukuda and W. Shang, "Automatic Sample Alignment Under Microscopy for 360° Imaging Based on the Nanorobotic Manipulation System," in *IEEE Transactions on Robotics*, vol. 33, no. 1, pp. 220-226, Feb. 2017.

[21] W. Shang, M. Zhu, H. Ren and X. Wu, "Centering of a Miniature Rotation Robot for Multi-Directional Imaging Under Microscopy," in *IEEE Transactions on Nanotechnology*, vol. 19, pp. 17-20, 2020.

[22] H. Lu, W. Shang, H. Xie and Y. Shen, "Ultrahigh-Precision Rotational Positioning Under a Microscope: Nanorobotic System, Modeling, Control, and Applications," in *IEEE Transactions on Robotics*, vol. 34, no. 2, pp. 497-507, April 2018.

[23] Fleming, Andrew J. and Kam K. Leang, "Design, Modeling and Control of Nanopositioning Systems," in *Switzerland: Springer International Publishing*, 2014.

[24] C. Ru, X. Liu, and Y. Sun. "Nanopositioning Technologies," in *Fundamentals and Applications*, 2016.

[25] S. Bashash and N. Jalili, "Robust Adaptive Control of Coupled Parallel Piezo-Flexural Nanopositioning Stages," in *IEEE/ASME Transactions on Mechatronics*, vol. 14, no. 1, pp. 11-20, Feb. 2009.

[26] H. C. Liaw and B. Shirinzadeh, "Neural Network Motion Tracking Control of Piezo-Actuated Flexure-Based Mechanisms for Micro-/Nanomanipulation," in *IEEE/ASME Transactions on Mechatronics*, vol. 14, no. 5, pp. 517-527, Oct. 2009.

[27] J. Zhong and B. Yao, "Adaptive Robust Precision Motion Control of a Piezoelectric Positioning Stage," in *IEEE Transactions on Control Systems Technology*, vol. 16, no. 5, pp. 1039-1046, Sept. 2008.

[28] Q. Xu, "Continuous Integral Terminal Third-Order Sliding Mode Motion Control for Piezoelectric Nanopositioning System," in *IEEE/ASME Transactions on Mechatronics*, vol. 22, no. 4, pp. 1828-1838, Aug. 2017.

[29] H. Tang, J. Gao, X. Chen, K. Yu, S. To, Y. He, X. Chen, Z. Zeng, S. He, C. Chen and Y. Li, "Development and Repetitive-Compensated PID Control of a Nanopositioning Stage with Large-Stroke and Decoupling Property," in *IEEE Transactions on Industrial Electronics*, vol. 65, no. 5, pp. 3995-4005, May 2018.

[30] W. Wei, Z. Zhang, M. Zuo, "Phase leading active disturbance rejection control for a nanopositioning stage," in *ISA Transactions*, vol. 116, pp. 218-231, Oct. 2021.

[31] Y. Wu and Q. Zou, "Iterative Control Approach to Compensate for Both the Hysteresis and the Dynamics Effects of Piezo Actuators," in *IEEE Transactions on Control Systems Technology*, vol. 15, no. 5, pp. 936-944, Sept. 2007.

[32] D. Meng and K. L. Moore, "Robust Iterative Learning Control for Nonrepetitive Uncertain Systems," in *IEEE Transactions on Automatic Control*, vol. 62, no. 2, pp. 907-913, Feb. 2017.

[33] H. Wang, J. Dong, Y. Wang, "High Order Feedback-Feedforward Iterative Learning Control Scheme with a Variable Forgetting Factor," in *International Journal of Advanced Robotic Systems*, vol. 13, no. 3, Jan. 2016.

[34] S. Liu, D. Xu, D. Zhang and Z. Zhang, "High Precision Automatic Assembly Based on Microscopic Vision and Force Information," in *IEEE Transactions on Automation Science and Engineering*, vol. 13, no. 1, pp. 382-393, Jan. 2016.

[35] Y. Yang, T. Li, X. Fu, Z. Sun, Y. F. Li and S. Liu, "Zooming-Free Hand-Eye Self-Calibration for Nanorobotic Manipulation Inside SEM," in *IEEE Transactions on Nanotechnology*, vol. 22, pp. 291-300, 2023.